Spatiotemporal Behavior of an Extremely Small Seismic Swarm in Pyrenean Foreland, France

Matthieu Sylvander, Sébastien Chevrot, Jean-Baptiste Ammirati, Sylvain Calassou, Magali Collin, Jordi Diaz, Nikos Martakis, Katerina Polychronopoulou, Antonio Villaseñor

BSSA (https://doi.org/10.1785/0120220263)

Spatio-temporal behavior of an extremely small seismic swarm in Pyrenean foreland, France

Matthieu Sylvander (1), Sébastien Chevrot (2), Jean-Baptiste Ammirati (2,3), Sylvain Calassou (6), Magali Collin (6), Jordi Diaz (4), Nikos Martakis (5), Katerina Polychronopoulou (5), Antonio Villaseñor (7)

1- IRAP, UMR 5277, Université de Toulouse, CNRS, CNES, UPS (Toulouse), France

2- GET, UMR 5563, Université Paul Sabatier, CNRS, IRD, Toulouse, France

3- Departamento de Geología, Universidad de Chile, Plaza Ercilla 803, 8320000, Santiago, Chile

4- Geosciences Barcelona, CSIC, Barcelona, Spain

5- Seismotech SA, Athens, Greece

6- TOTAL EP/R&D, Pau, France

7- Institut de Ciències del Mar, Barcelona, Spain

Corresponding author

Matthieu Sylvander, Observatoire Midi-Pyrénées, 14 avenue Edouard Belin, 31400 Toulouse, France. Phone +33 5 61 33 29 82. E-mail msylvander@irap.omp.eu

Declaration of Competing Interests

The authors acknowledge there are no conflicts of interest recorded.

Abstract (227 words)

During the large-N Maupasacq passive seismic experiment in the foreland of the western Pyrenees (SW France), an unusual swarm-type seismic sequence was serendipitously recorded in a normally quiet area. Thanks to the density of the deployment and the proximity of all events, it was possible to relocate the hypocenters with a very good relative accuracy through template matching, cross-correlation phase picks and double-difference algorithm. The 4-month seismic activity consists of more than 600 events with local magnitudes ranging between -1.4 and 2.1, clustered in an extremely small volume, rooted at 4 km depth. The sequence can be divided in two phases of similar durations and event occurrence rates, but different magnitude-frequency distributions. The presence of an asperity is suggested by the relative abundance of stronger events during the second phase. Fine mapping suggests a small but clear geographic offset of a few tens of meters between the events of the two phases, and a very slow migration suggesting a process involving fluids. Changes in the correlation matrices and waveforms of late arrivals at a specific station are also observed, arguing either (and again) for migration of the hypocenters, or for changes in the propagation medium between the two phases. The geographical coincidence with the repeated observation of hydrogen leaks on the surface, almost above the swarm, suggests a connection through channels that could carry fluids.

1 Introduction

Seismic swarms are sequences of numerous earthquakes occurring over a relatively short period of time (typically days to months), not specifically preceded by a mainshock, and contained within a relatively small volume (e.g. Hill, 1977). Seismic swarms have been observed in a variety of settings: tectonic, volcanic (e.g. Wyss et al., 1997; Dreger et al., 2000), geothermal (e.g. Duboeuf et al., 2022) or in contexts of hydrothermal alteration (e.g. Heinicke et al., 2009). They have often been linked to fluid migrations, either directly or through the intermediary of fluid-induced aseismic slip (e.g. Fischer et al., 2014; de Barros et ail., 2019, 2020; Wei et al., 2015) although the mechanisms controlling swarm activity, especially how they begin and when they stop, are not certain. The general idea is that a swarm is related to the activation of a mesh of small fractures under increasing fluid pressure but without sufficient coherence among the mesh for the rupture to propagate and generate a large event (as modelled by Yamashita, 1999). This is why seismic swarms are generally characterized by low-magnitude earthquakes.

Although seismic swarms can be either of natural or anthropogenic origin (e.g. fluid injections), the mechanics controlling the swarm dynamics are believed to be the same and seem to be associated with pre-existing zones of weakness (Mogi, 1963; Fischer et al. 2014). Because seismic swarms are mostly characterized by small magnitude earthquakes, their characterization requires nearby instrumentation. Furthermore, except in specific cases of monitored anthropogenic fluid

injections, the erratic nature of naturally occurring swarms requires a fair amount of luck, i.e., the right network, in the right place, at the right time, to be able to detect and characterize them correctly.

In this work, we analyze a swarm sequence of 615 earthquakes recorded during the MAUPASACQ experiment, a large-N array deployed in the Mauléon basin (French Pyrenees) from April to October 2017.

2 The Maupasacq experiment

Located north of the Pyrenean range (SW France), the Mauléon basin is an ancient hyper-extended rift, inverted during the Pyrenean (Alpine) orogeny (e.g. Jammes et al., 2009; Mouthereau et al., 2014; Masini et al., 2014; Fillon et al., 2020; Lescoutre and Manatschal, 2020). It is characterized by a strong positive gravity anomaly (Fig. 1), most likely caused by a wedge of mantle material exhumed during the Cretaceous episode of rifting, which has been imaged by both receiver function analysis and full waveform inversion of teleseismic P waves (Wang et al., 2016; Chevrot et al., 2018; Chevrot et al., 2022). The Maupasacq experiment (standing for MAUléon PAssive Seismic ACQuisition) aimed at imaging this structure through a passive seismic survey (e.g. Polychronopoulou et al., 2018; Chevrot et al., 2022). A network of 452 three-component seismic stations (broad-band, short-period and geophone nodes) was deployed and maintained in a 50x30 km² area for 6 months (April-October 2017). The underlying idea was to quantitatively assess the imaging capabilities of a dense passive deployment, in a region with a clear scientific challenge, and where a profusion of available geological logs and seismic sections would provide strong independent constraints. The overall experimental set-up is described in Supplemental Material.

Several studies have been so far dedicated to the exploitation of the data set collected or are still under way, among which the inversion of a 3-D shear velocity model based on the extraction of coherent surface wavefronts from ambient seismic noise (Lehujeur et al., 2021), a classical local ambient noise tomography (Boué et al., 2019), or a local earthquake tomography (Villaseñor et al., 2019; Lehujeur et al., 2021). In particular, the different tomographic models clearly outline a body characterized by very high velocities, which corresponds to the mantle wedge revealed by Wang et al. (2016). The results demonstrate the capabilities of this kind of deployment to image with a fine resolution crustal structures at the local scale.

As a prerequisite for some of the imaging goals of the experiment, the local seismicity was studied in detail using a classical semi-automatic approach. P-wave picks were obtained following the method outlined by Tselentis et al. (2011), which consists in applying the Kurtosis criterion after denoising the record through filtering in the S-transform domain. S-wave arrival times, which are

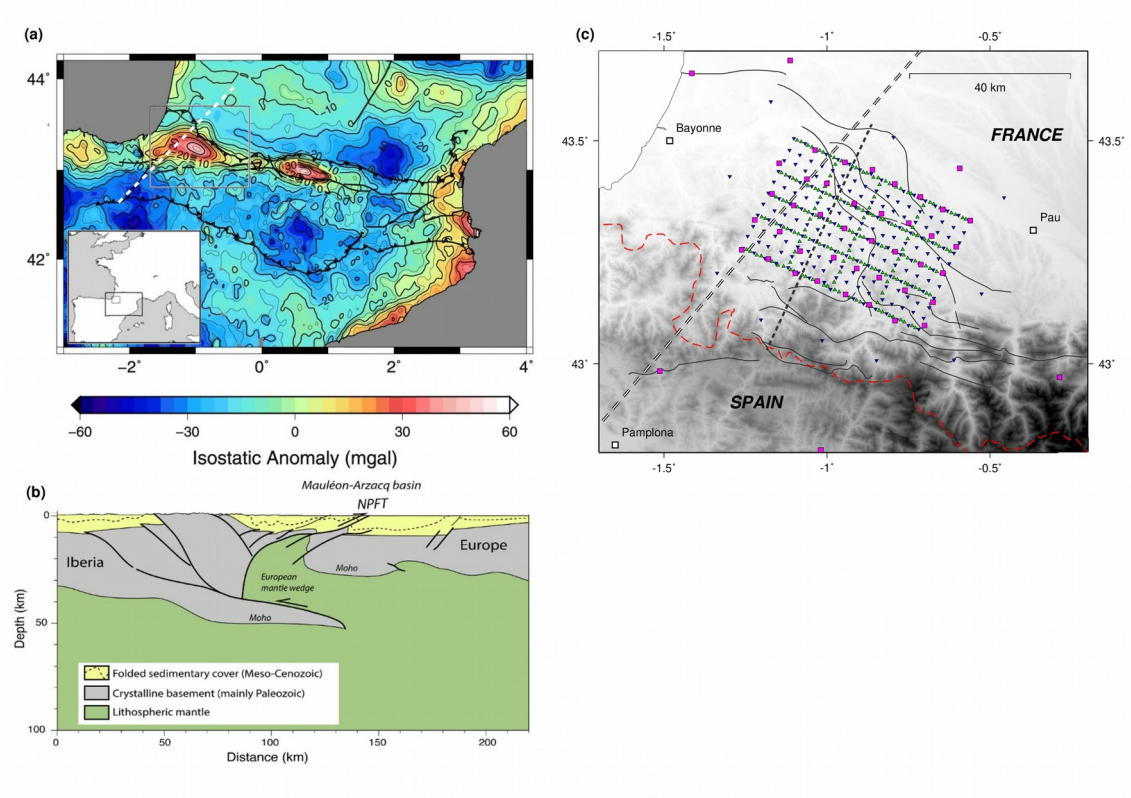

Figure 1. (a) Isostatic anomaly map of the Pyrenees (SW France / NE Spain). The grey frame corresponds to the blowup of panel c, and shows the prominent positive isostatic anomaly of the Mauléon basin. The map is adapted from Chevrot et al (2018). White dashed line corresponds to cross-section of next panel. (b) Northeast-Southwest cross-section through the Western Pyrenees, showing the shallow wedge of mantle material trapped in the crust (from Wang et al., 2016) and responsible for the isostatic anomaly shown in panel a. (c) Station map of the Maupasacq experiment. Pink squares: broadband sensors; blue inverted triangles: short period sensors; green triangles: nodes. Faults are taken from Saspiturry et al. (2019). White dashed line corresponds to cross-section of panel (b). Grey dashed line corresponds to cross-section of Fig. 12.

often more difficult to pick, were obtained using the time-domain approach described by Lois et al. (2013), based on computing a characteristic function from eigenvalues. After picking phases at all stations in the network and associating arrival times, hypocentral positions were obtained by running the Hypo71 software (Lee and Lahr, 1975), resulting in a catalog of 1748 local earthquakes. Local magnitudes (M_{Lv}) were calculated in an usual way, on the maximum amplitude around the S-arrival of the signal converted to displacement, and scaled to the magnitudes that are in use on the French territory as described by Duverger et al. (2021).

Figure 2 shows the overall seismicity map for the whole Maupasacq experiment. It is largely consistent with the current knowledge of the local seismic activity, that results from decades of monitoring with a permanent, though much sparser network (Souriau and Pauchet, 1998; Souriau et al., 2001 ; Lacan and Ortuño, 2012; Sylvander et al., 2021). Of course, this similarity in the distribution of earthquakes is purely qualitative, as the density of the device has allowed us to locate approximately 15 times more events than the permanent monitoring network over the same period (1748 against 120) using a conventional semi-automatic approach. It should be noted that

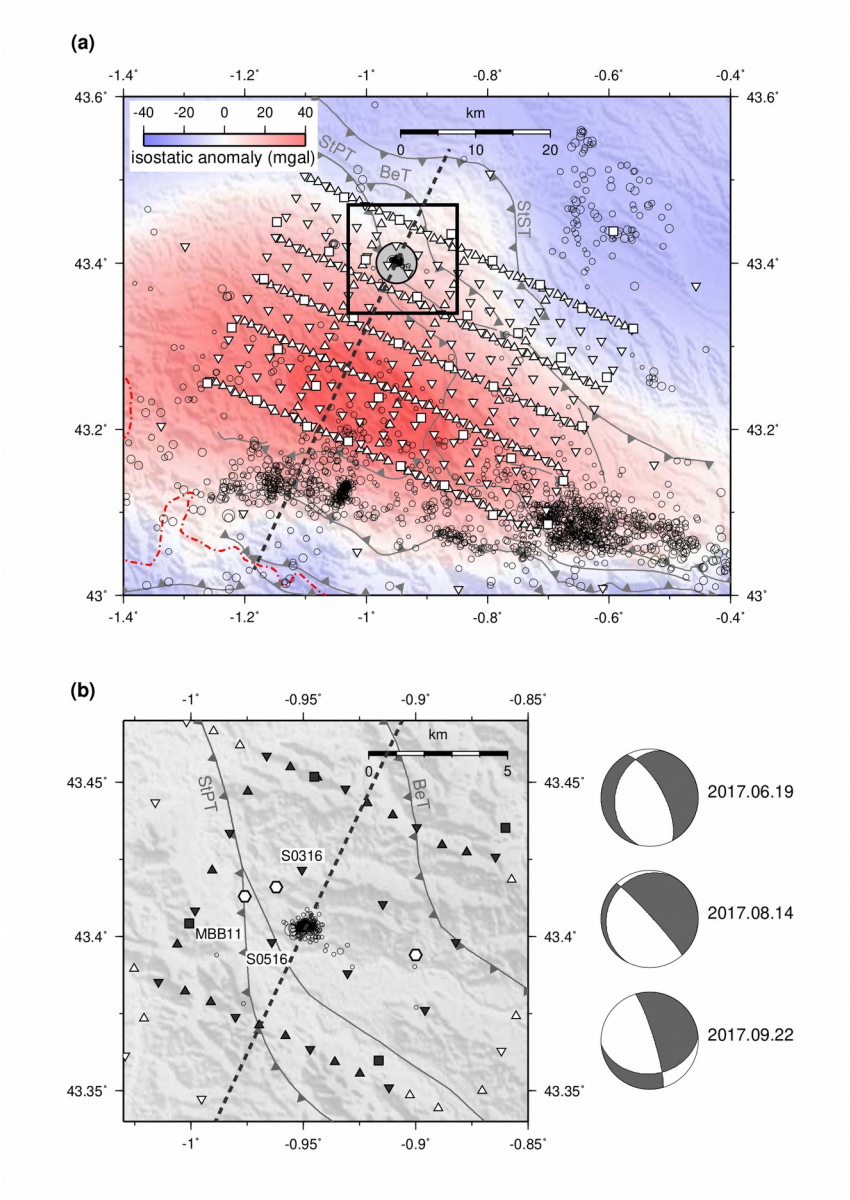

Figure 2. (a) Epicenter map after the initial location procedure, superimposed on the gravity map. Empty circles: earthquake epicenters; size is proportional to magnitude. Squares: broadband sensors. Inverted triangles: short period sensors. Triangles: nodes. Faults from Saspiturry et al. (2019). St-Pt: Saint-Palais Thrust. St-ST: Sainte-Suzanne Thrust. BeT: Bellevue Thrust. The dashed line corresponds to the interpretative cross-section of figure 12. (b) Close-up on the swarm (initial location). Filled symbols mark stations that were used for the accurate relative relocation. Three stations mentioned in the text are labeled. White hexagons correspond to events from the 40-year regional catalog of Sylvander et al. (2021). The three representative mechanisms are the same as in the top row of figure 11. The first one is for the master event of the sequence (2017.06.19-07:43).

the activity of these 6 months is representative of the standards, the semi-annual average (over several decades) of the number of earthquakes in the study zone amounting to 130 in the permanent catalogue (Sylvander et al., 2021).

However, the purpose of the present article is not to discuss the seismicity of the entire area, but to focus on a particular seismic sequence. Indeed, the exceptional density of the Maupasacq

device allowed the recording of a very unusual seismic swarm, without precedent in the local catalogues. This sequence, hereafter referred to as the Sauveterre swarm (named after the nearby town), occurred in a part of the basin where very few events had been detected in the previous 40 years (from the file gathered by Sylvander et al., 2021). The early processing described earlier identified and located 212 events between May 2nd and September 2017, concentrated over two square kilometers, with depths also highly concentrated (mean 3.7 km, standard deviation 1.6 km). This exceptional clustering of earthquakes, in a region until then considered practically seismically inactive, motivated a dedicated study to refine the location, spatial extent and behavior of the sequence.

3 The Sauveterre swarm: template matching methods, relative locations and results

As could be expected from such clustered seismicity, the waveforms of the events are remarkably similar. Figure 3 shows the vertical component seismograms of a number of events from the swarm recorded at a closeby station (S0516, short-period sensor). They reveal secondary seismic phases that are probably related to conversions/reflections. A fine study of these phases should provide new constraints on the position of local interfaces/structures such as the basement or the North Pyrenean Frontal Thrust and its local branches (St-Palais thrust, Ste-Suzanne Thrust, Bellevue Thrust, see for instance Saspiturry et al., 2019). The striking similarity of these waveforms led us first to launch a complementary search for signals that would have escaped the initial analysis, and then to perform a relative relocation by double-differences, based on high precision differential phase picks measured by cross-correlations.

3.a Template matching

Given the exceptional profusion of stations at short distances from the swarm, we chose to restrict their number, and thus the range of epicentral distances, in order to limit 3D propagation effects due to the heterogeneity of the medium. We limited ourselves to the 35 closest stations, which means that in the following analysis, the swarm is surrounded by a rectangular mesh with a maximum epicentral distance of about 8 km (see Fig. 2b). The search for additional events was performed by a classical template matching procedure based on Obspy routines (e.g. Krischer et al., 2015) and applied to the three components of the 35 stations, bandpass filtered between 4 and 20 Hz. We chose as template an event that was recorded by as many stations as possible, with a good signal-to-noise ratio. Several candidates were tried, and the one that gave the best final results in terms of the number of additional events identified was selected (2017.07.21-21:44:11, M_L=0.6). The correlation search was performed on 6 seconds of the template signal, starting from the origin time. At the distances considered, this window length ensures that the entire signal of interest, from the P arrival to the beginning of the S coda, is taken into account, even for low

propagation velocities in the thick sediment layer. The threshold for the correlation coefficient was chosen by examining the trade-off curve between the correlation coefficient and the number of

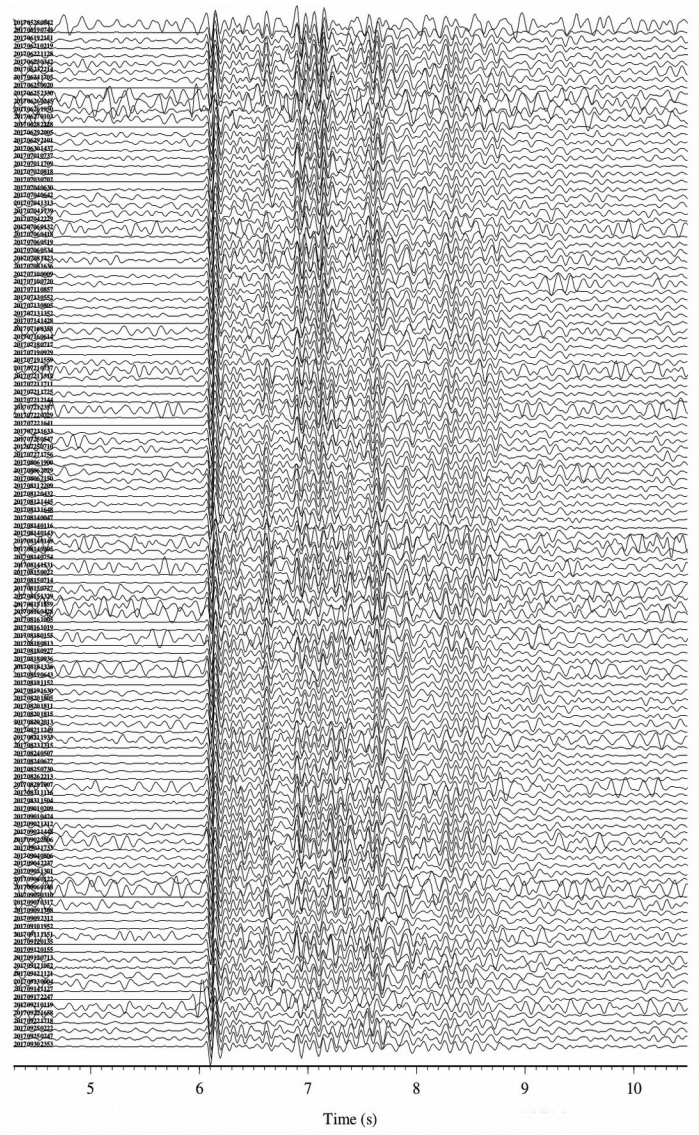

Figure 3. Waveforms of the Sauveterre swarm events (initial processing, before template matching) recorded at station S0516, 2.2 km away from swarm centroid. Vertical component of short-period velocimeter, bandpass filtered between 4 and 15Hz. The waveforms are arranged in chronological order (earliest at the top), normalized to the amplitude of the P-wave and aligned to origin time.

matches on the three components of the signal. A value of 0.50 was retained, above which the number of matches increases exponentially. Note that at this stage, false detections are numerous, the trade-off curve having only a statistical purpose. This procedure led to 1500 composite (3-component) matches, defined as the coincidence, in a conservative 3 second time window, of individual matches (at 0.50 correlation level) in at least 3 stations (in order to be able to locate the earthquakes). Again, this sorting was not drastic enough to eliminate false detections. The last step of the screening consisted in performing a preliminary localization (with Hypo71) which allowed to keep only the detections corresponding to events of the swarm. The waveforms of the 613 events

(final number) retained but seen by a small number of stations (5 and less) were individually inspected in order to confirm their visual resemblance with the template.

3.b Magnitude calculation

For the additional events, which now represent two-thirds of the final « Sauveterre swarm » catalogue, we computed MLv magnitudes consistent with the magnitude values of the initial processing. For this, we used the fact that the distances between the events and the stations are always the same within a few tens of meters (see Fig. 4), as well as the radiation patterns (because of the similarity of the waveforms). Starting from the magnitudes of the initial processing, we could therefore compute, for each station, average constant terms that account simultaneously for the distance correction, the site correction, and the instrumental response (equation 1; the summation is done on the N_e events for which a magnitude has been calculated in the initial processing; C_i is the average constant term for station i, M_j is the magnitude for event j, A_{ij} is the maximal displacement recorded at station i for event j).

$$C_i = \frac{1}{N} \sum^{N_e} \left(M_j - logA_{ij} \right) \qquad (1)$$

These constant terms could in turn be reinjected in the calculation of the magnitudes for the additional events, for which we only needed to compute the maximal displacement around the S-arrival (equation 2; the summation is done on the N_s stations that recorded additional event i ; M_i is the magnitude for additional event i, A_{ji} is the maximal displacement recorded at station j for event i).

$$M_i = \frac{1}{N} \sum^{N_s} \left(logA_{ji} + C_j \right) \qquad (2)$$

The main advantage of this procedure is that the instrumental responses do not need to be known precisely, which is a real asset for such a heterogeneous instrumental setup. Of course, this is only possible because of the similarity of the events, which is guaranteed by their identification through template-matching. The calculated magnitudes are by construction consistent with the French MLv local scale described by Duverger et al. (2021). They range between -1.4 and 2.1.

3.c Double-difference relocation of seismicity

Cross-correlation based differential phase picking (P and S waves) was performed on the initial data set and on the additional events identified by template matching, for a total of 613 events. The exceptional profusion of events and nearby recording stations led us to retain only those stations located within an epicentral distance of 10 km from the cluster centroid. The total number of differential times resulting from the cross-correlations is more than 700000 (222000 P differential times, 485000 S differential times). The larger number of S times reflects the very low magnitudes of the events identified by template matching: 80 % are below magnitude 0.0, only 3 % above 1.0.

A double-difference HypoDD relocation procedure (Waldhauser, 2001; Waldhauser and Ellsworth, 2000) was then run, including the catalog picks from the initial processing (194000 P- and 187000 S differential times). In total, more than 1 million differential travel times were thus used to relocate the overall sequence. Many runs were performed to converge on « best » inversion parameters, as evaluated mainly from the continuous decrease of the root mean square on the catalog and cross-correlated differential times in the iterative process (WRCC, WDCC, WRCT, WDCT parameters in the weighting and re-weigthing scheme, see Waldhauser, 2001), while adjusting damping to keep the condition number in the recommended range (40 < CND < 80). The final data set consists of 481 relocated events. About a quarter of the events could therefore not be relocated; visual inspection of their recordings shows that they are always very low magnitude events, captured by three stations at most, and for which the noise level prevents accurate picking.

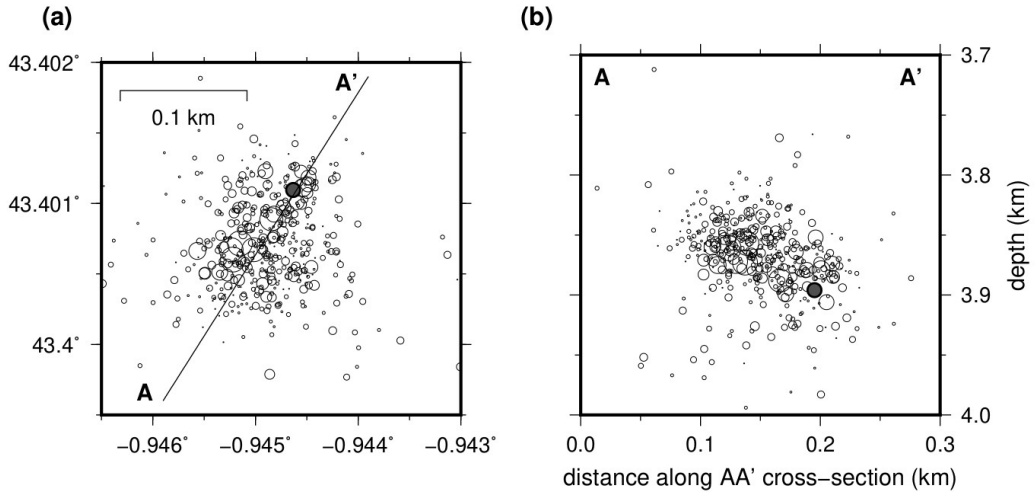

Figure 4. Fine mapping of the sequence (after template matching, cross-correlation picking and double difference relocation – see text). (a) map view. (b) AA' cross-section. Symbol size is proportional to earthquake magnitude. The gray circle with bold contour corresponds to the master event of the sequence (2017.06.19-07:43).

Figure 4 displays the results of the double-difference relocation procedure in map view and in a cross-section perpendicular to the nodal planes of the main focal mechanisms (see section 3.e). The clusters appears to be extremely concentrated, with more than 400 events spanning 3 orders of magnitude packed into a roughly spherical volume 150 m in diameter. Note that this implies an upper bound 0.15 x 0.15 = 0.0225 km² rupture area (whatever its orientation), which fits reasonably well with the M = logA + 3.98 scaling law proposed by Hanks and Bakun (2002). Applying this relationship on the M = 2.1 maximum magnitude of the sequence, we indeed obtain a rupture surface of 0.013 km². The concentration of events, as measured by the standard deviation of the distances of individual events to the barycentre of the swarm, is reduced by a factor of ten between

the set of initial locations (σ = 488 m) and the accurate dataset built by template matching and double difference locations (σ = 52 m). In order to assess relocation uncertainties, we performed a jackknife analysis by randomly setting aside 20 % of the picks over a hundred draws, and we calculated errors, meant as the standard deviations in the two horizontal and the vertical directions to the mean locations obtained through this jackknife process. Average errors are close to 10 m (9.1 ± 5.3 m in latitude, 11.1 ± 4.8 m in longitude, 8.2 ± 5.8 m in depth), which will ensure the significance of the interpretations that follow.

3.d Temporal behavior: two distinct phases and migration analysis

Figure 5 (top) displays the chronology of the Sauveterre sequence. After a few early events in late April and May and a quiescence of 40 days, the sequence really starts on 2017.06.19 with what we will call the « master event » (2017.06.19-07:43, M_L=1.0). Two very distinct phases are

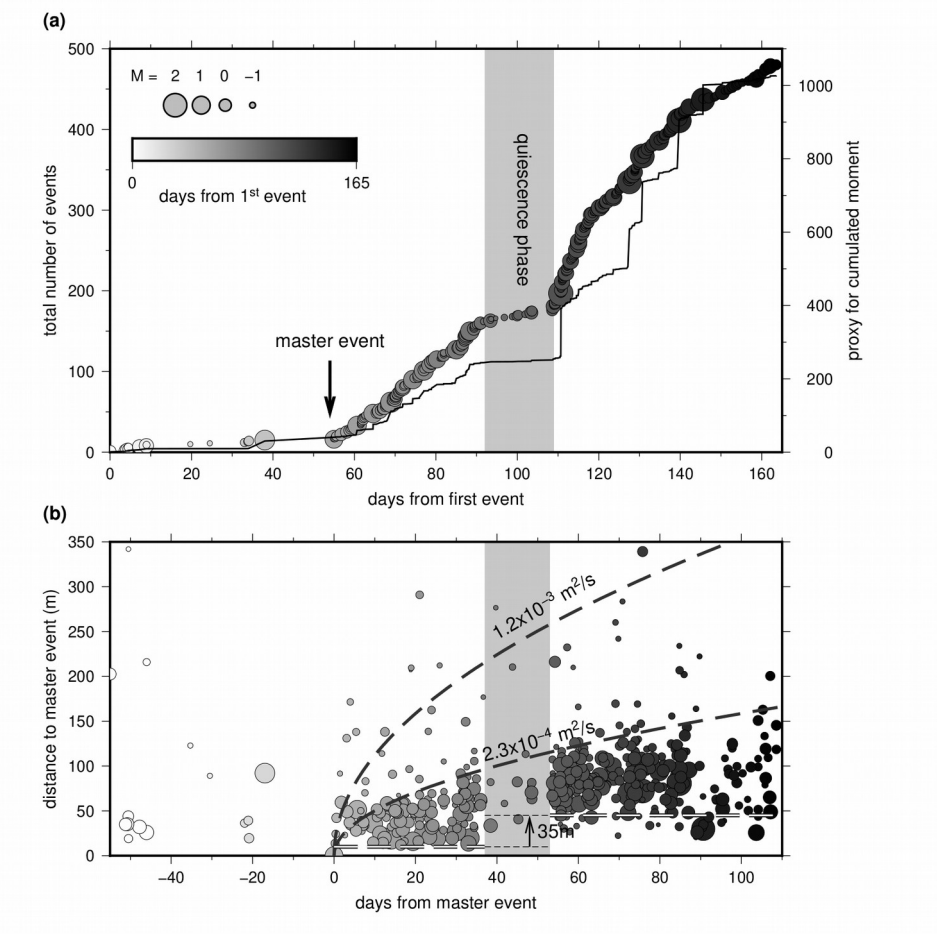

Figure 5. (a) Chronology of the sequence, from the initial onset (2017.04.29) to the dismantling. Only the 481 events that could be relocated with HypoDD are plotted. The plain line represents a proxy for cumulated moment (sum of individual 10^{ML}). The timing of the so-called “master event”, is plotted. The grey vertical band marks the quiescence phase (see text). (b) Representation of migration as a diffusion process. The dataset is the same as earlier. Distance and time refer to the master event (2017.06.19-07:43). Dashed envelopes represent diffusion curves with high and low diffusivity values. Horizontal dashed lines mark the overall spatial shift between hypocenters of the two phases.

separated by a pause of nearly 2 weeks. Figure 5 (bottom) presents in a classical way the evolution of the distance to the master event as a function of the elapsed time since this event. We can see a clear although extremely limited geographic migration over time. Note that the second phase of the sequence, which begins ~50 days after the master event, starts with an overall step of about 35 meters, at a significant level considering the accuracy of the event locations. This can also be seen in Fig. 6, in which the events of the two phases delineate two overlapping patches, but nevertheless confirm the observation of an overall displacement of seismicity of about thirty meters to the southwest and upward, rather than a progressive and regular migration over time. Therefore, the two phases seem to involve two slightly different geographical patches. If we however attempt to model the migration with a classical diffusion law of the type $r=\sqrt{4\pi Dt}$ (ignoring here the difference between the two phases), the diffusivity constant obtained is in the order of 2.10^{-4} m^2/s (Fig. 5, bottom).

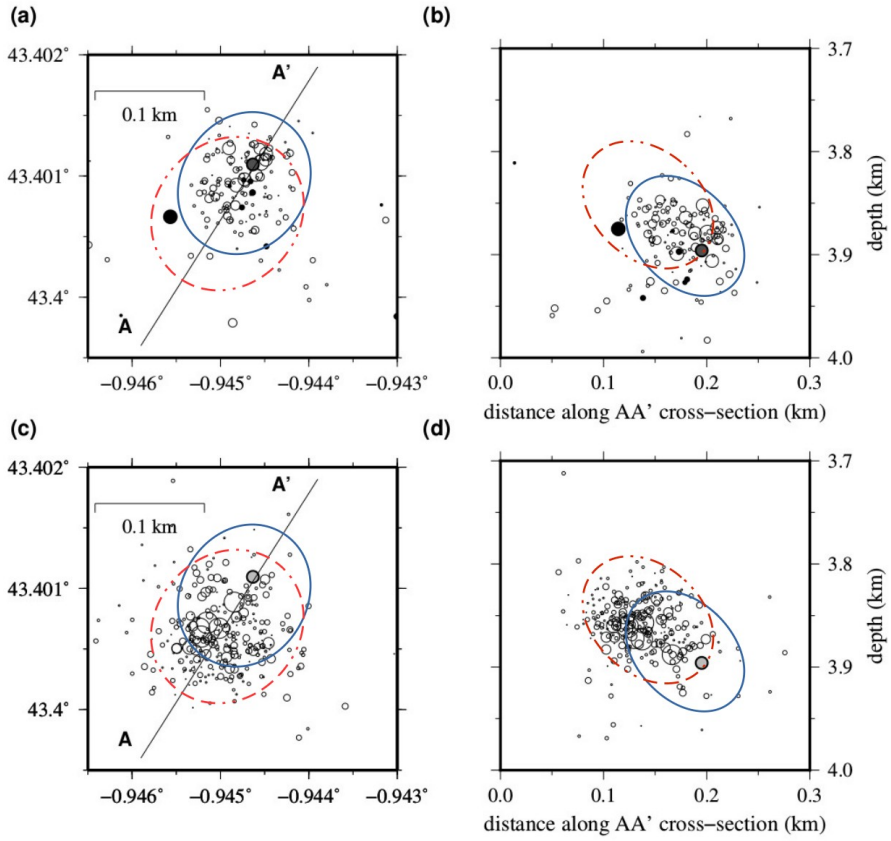

Figure 6. (a) and (b) Same as figure 4, but with only early events (black circles, before day 54) and phase 1 events (empty circles, between days 54 and 93). Plain blue and dashed orange ellipses: approximate contours of phases 1 and 2. (c) and (d) Same as (a) and (b), but for phase 2 events only (later than day 107). The gray circle with bold contour corresponds to the master event of the sequence (2017.06.19-07:43).

These two phases show similar event occurrence rates, but different frequency-magnitude distributions (Fig. 7). The second one shows a much higher proportion of “strong” events,

suggesting a more pronounced asperity-like behaviour than in the first phase. Note that the two sequences do not show very regular Gutenberg-Richter like distributions. One might be tempted to attribute this to the relatively small number of events in each phase (150 for the first phase, 288 for the second one). However, it may be noted that common practice in the field of frequency-magnitude distributions is rather permissive in this respect. For example, the developers of the ZMAP software (e.g. Wiemer and Wyss, 1997, 2000), which is the reference in the calculation of this type of statistic, forbid themselves to invert a value of b as soon as the number of events in their data set is smaller than 50. Here, we have between 3 and 6 times more points, which gives us confidence in our analysis. There is no clear mainshock/aftershocks pattern, which unambiguously classifies this Sauveterre sequence in the “swarm” category (e.g. Vidale and Shearer, 2006; de Barros et al., 2019). The three largest events reach magnitude values of 2 to 2.1, all during the second phase of the sequence. The end of this second phase can unfortunately not be ascertained, because of the dismantling of the experiment.

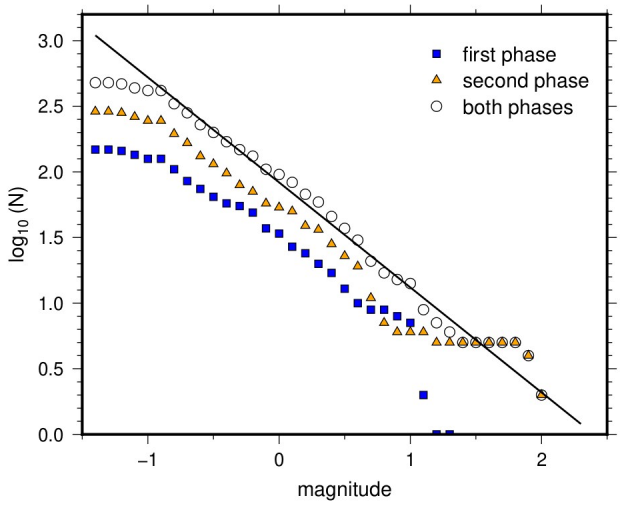

Figure 7. Frequency magnitude distribution for the two phases of the Sauveterre sequence. Blue squares: phase 1 (between days 54 and 93, starting from first event). Orange triangles: phase 2 (from day 108). Open circles: overall sequence (two phases gathered). A slope of 0.84 is obtained by line fitting of the data for both phases.

Since the existence of these two phases is a very intriguing observation, we tried to confirm it by finely exploring the similarities of the events. To do this, we first gathered the information given by the waveform similarity, by computing correlation matrices.The seismograms were correlated within 1.5 s wide windows around the P-wave (0.5 s before the theoretical arrival and 1.0 s after). Figure 8 shows the correlation matrix for station S0316, located 2.3 km NNW of the swarm. There is a clear separation of this matrix into two squares, with stronger cross-correlations within the two subsets of events. Not surprisingly, these two subsets correspond to the two phases described earlier. This dichotomy was searched for at other nearby stations (within 5 km from the swarm), and are indeed observed, but to a lesser extent, only at one station, S0516 (2.5 km SSW of the

swarm). This is probably due to the fact that the correlations are computed on the very first P-arrival and that the events migrate in a direction close to the azimuth of stations S0316 and S0516, making small geographical offsets more likely to be detected on the correlation matrix at these stations. Note that this strongly suggests a global movement between phase 1 and phase 2 rather than a continuous migration.

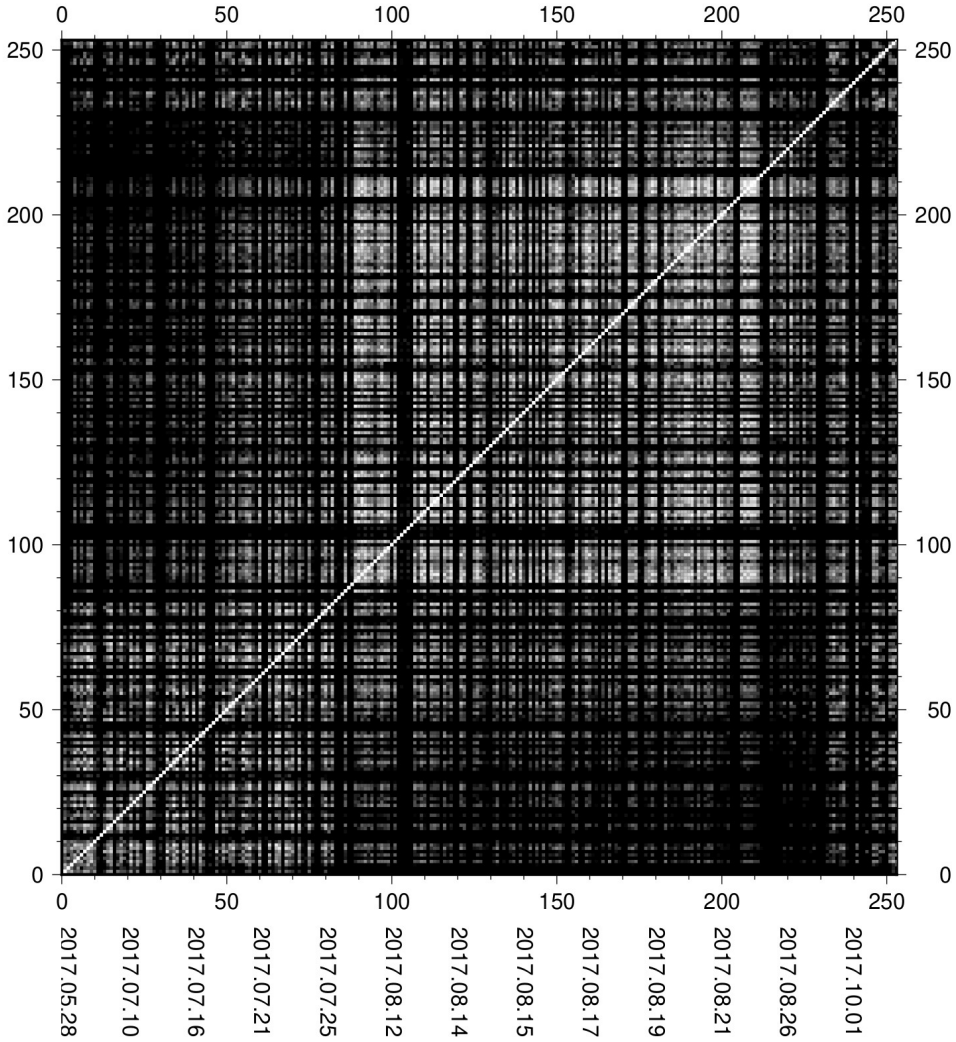

Figure 8. Correlation matrix for station S0316. Colors reflect the cross-correlation coefficient between first P arrivals of distinct events (from black = 0.7 and below, to white = 1.0). Correlations are performed on the three components of the sensor, filtered between 4 and 20 Hz, and the maximum value is displayed. Numerals on the axes are the sequence numbers of the earthquakes. Note the division in two separate squares for the two phases revealed in figures 5 and 7 (bottom left: phase 1; top right: phase 2).

We then took a closer look at the three-component waveforms recorded at station S0316. On figure 9, we can clearly observe, on a selection of events with good S/N ratios, an evolution of these waveforms over time, mainly on the late arrivals. In particular, the transition from one stage to the other is accompanied by the disappearance of the phase marked as X on the East component (which corresponds within 12 degrees to the transverse direction). Surprisingly, the

opposite phenomenon occurs on the vertical component, at the same onset time. We can also observe on the North component (equivalent to the radial component) a temporal drift of the arrival that precedes it. These two energy packets seem to arrive earlier and earlier during the first period of the sequence. The stacked seismograms show that on all components, the P and S arrivals are similar from one period to another, while the later arrivals show a phase shift. Figure S1 in the Supplemental Material shows in a different form (normalized envelopes) that the bulk of these observations also emerges when the whole set of events detected by template matching is taken into account.

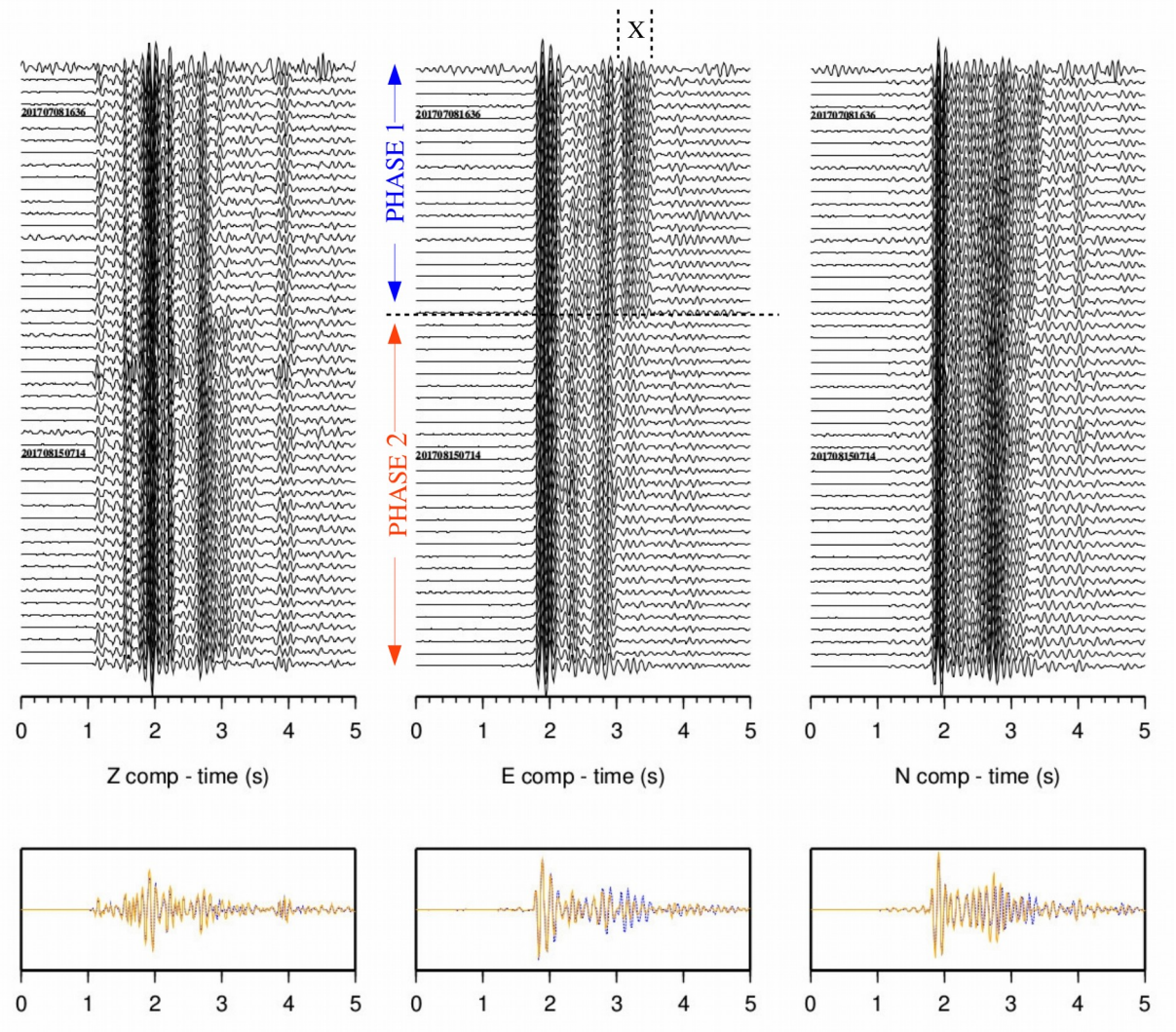

Figure 9. Top: Three-component velocity waveforms of selected events (with good S/N ratio) at short-period station S0316, bandpass filtered between 4 and 15Hz. The waveforms are arranged in chronological order (earliest at the top), normalized to the maximum amplitude of the trace and aligned to origin time. Backazimut is ~168°, therefore component E is almost in the horizontal-transverse direction, whereas component N is almost in the horizontal-radial direction. The main change in waveforms over time can be seen on the E component, on the arrival labeled X (shortly after 8 s). Dates correspond to specific events (one per phase) for which the polarization of arrival X is displayed on figure 10. Bottom: stacked waveforms for the events of phase 1 (dashed blue) and phase 2 (orange). All the events detected by template matching are stacked (see also Fig. S1).

Particle motion plots (Fig. 10) performed on L, Q, T rotated components of selected events confirm unambiguously that this X arrival is strongly polarized as a SH wave during the first phase (from the linearity of the Q/L and T/L diagrams, and the much greater amplitude on the T component), and switches to an almost perfect mix of SV and SH energy during the second phase (from the ellipticity of the T/Q diagram). This observation will be discussed later.

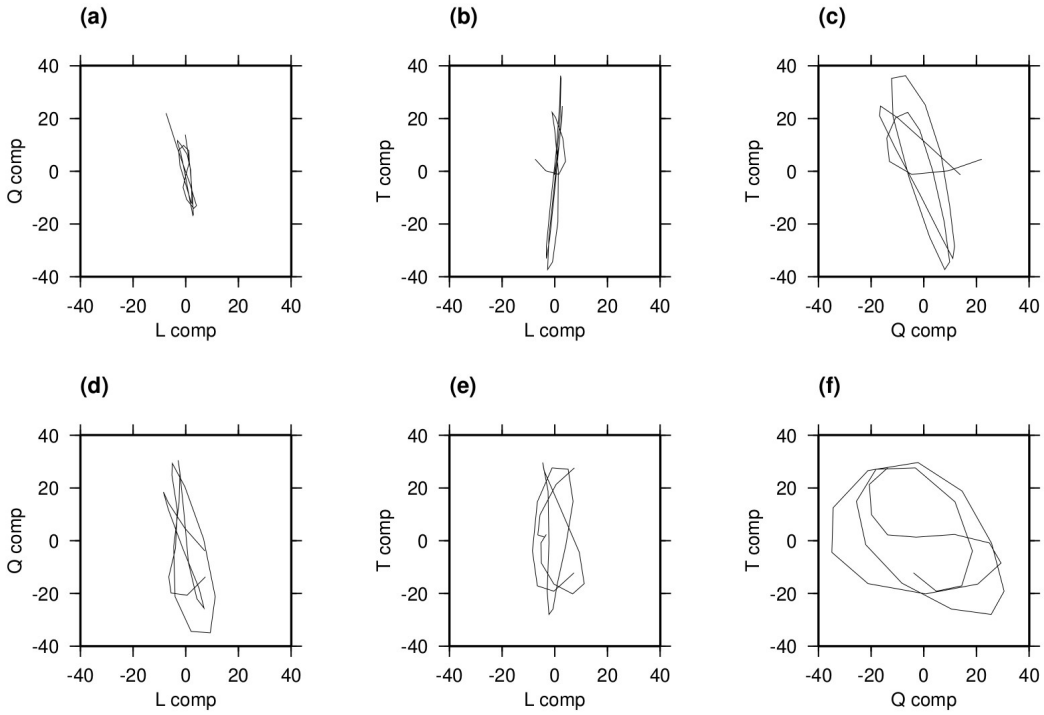

Figure 10. Particle motion plots for the arrival labeled X (see Fig. 9). The 0.35s long time series have been 3D-rotated to the L, Q, T referential of the seismic ray. Top (a,b,c): typical event for phase 1 (2017.07.08-16:36, ML=1.0). Bottom (d,e,f): typical event for phase 2 (2017.08.15-07-14, ML=0.6). (a) and (d) Q/L diagrams. (b) and (d) T/L diagrams. (c) and (e) T/Q diagrams. The amplitudes are expressed in relative units (same scaling for each component of a given event, i.e. on a row).

3.e Focal Mechanisms

Table 1 and figure 11 show the focal mechanisms for a selection of events spread over the entire seismic sequence. The high density of stations allows for excellent azimuthal coverage, which provides the possibility to determine reliable focal mechanisms based on polarities for low magnitude events. Focal solutions were computed using the FOCMEC package (Snoke, 2003) with P polarities only. Because of the small size of these earthquakes, it is difficult to draw seismotectonic implications from them. In fact, despite the proximity of the events and the strong waveform similarities, we observe significant fluctuations of the focal solutions but nevertheless they are all extensional mechanisms, with one nodal plane close to the vertical and, for the most part, sub-parallel to the local faulting system. There is no apparent difference in the mechanisms between the two phases of the sequence (i.e. at the transition between July and August). The

presence of extension may appear surprising at first glance in a local context of thrusting (as advocated by the presence of the North Pyrenean Frontal Thrust and its local branches). However, the generalized presence of extension is well documented in the entire Pyrenean domain (e.g. Chevrot et al., 2011 ; Mazzotti et al., 2021), and generally explained by isostatic readjustments following the cessation of the Eurasia/Iberia convergence, as evidenced by the negligible horizontal deformations observed by GNSS, either from campaign surveys (Asensio et al., 2012, Rigo et al., 2015), or from permanent station records (Nocquet, 2012, Masson et al., 2019).

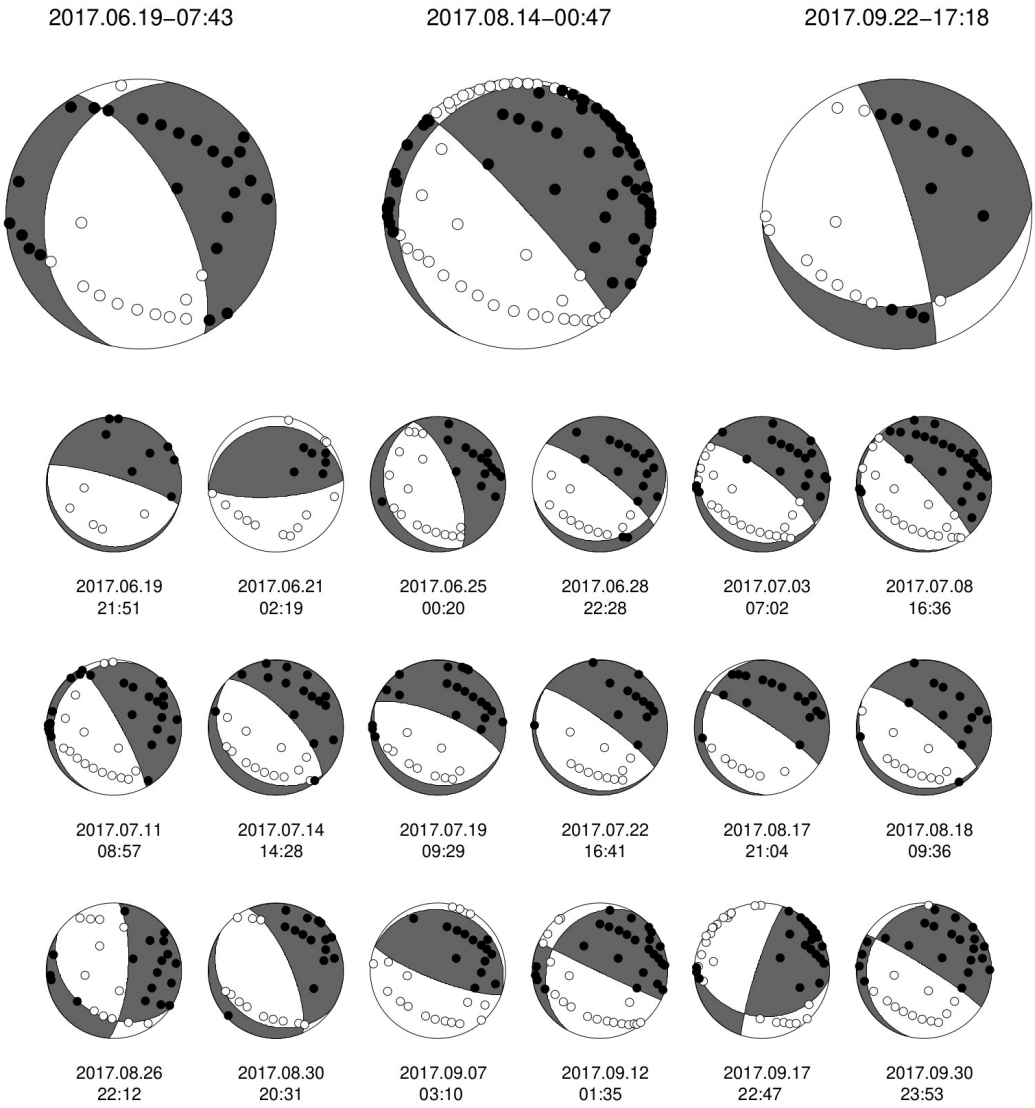

Figure 11. Focal solutions (first motion polarities) for a selection of events (see Table 1). The three highlighted mechanisms of the top row correspond to events of the first phase (master event), early second phase and late second phase. The density of individual polarities gives an idea of the resolution of these mechanisms.

Table 1. Characteristics of the focal mechanisms for all events of figure 11. The events in the first three rows correspond to the first three beachballs of figure 11. Highlighted in grey are the subvertical nodal planes, common feature of all the mechanisms.

Origin time	Latitude	Longitude	Depth	Mag	Str1	Dip1	Rk1	Str2	Dip2	Rk2
20170619-07:43	43.401095	-0.944633	3.896	1.0	193	30	-53	332	66	-109
20170814-00:47	43.400716	-0.945152	3.873	2.0	206	13	-22	317	85	-102
20170918-17:22	43.401127	-0.945270	3.902	0.4	86	32	-165	343	82	-59
20170619-21:51	43.401119	-0.944475	3.856	-0.4	107	9	-90	287	81	-90
20170621-02:19	43.400972	-0.945012	3.847	0.1	266	15	90	86	75	90
20170625-00:20	43.401229	-0.944904	3.852	1.1	159	22	-90	339	68	-90
20170628-22:28	43.400972	-0.944727	3.864	1.1	77	18	-139	307	78	-76
20170703-07:02	43.401111	-0.944542	3.879	1.4	112	16	-105	307	75	-86
20170708-16:36	43.401135	-0.944487	3.906	1.1	157	7	-70	317	83	-92
20170711-08:57	43.400924	-0.944819	3.899	1.2	201	12	-41	331	82	-99
20170714-14:28	43.401225	-0.944557	3.885	0.9	131	21	-95	317	69	-88
20170719-09:29	43.401184	-0.944484	3.874	1.1	112	17	-90	292	73	-90
20170722-16:41	43.401009	-0.944598	3.879	1.1	126	9	-90	306	81	-90
20170817-21:04	43.400484	-0.944627	3.849	0.7	175	13	-39	303	82	-100
20170818-09:36	43.400765	-0.944819	3.854	0.8	113	12	-104	307	78	-87
20170826-22:12	43.400549	-0.944455	3.834	0.9	123	32	-147	4	73	-62
20170830-20:31	43.400671	-0.945017	3.857	2.0	125	21	-120	337	72	-79
20170907-03:10	43.400513	-0.945348	3.860	1.2	291	11	90	111	79	90
20170912-01:35	43.400602	-0.945220	3.861	2.1	209	24	4	115	88	114
20170917-22:47	43.400887	-0.944845	3.888	1.9	97	33	167	199	83	58
20170930-23:53	43.401074	-0.944495	3.873	0.7	193	16	-20	302	85	-105

4 Discussion

The exploration of the 40-year catalogue gathered by Sylvander et al. (2021) retrieved 10 events located within 10 km of the Sauveterre swarm, three of which appear on figure 2b. However, we note that until 2019, the local monitoring network was not able to guarantee completeness below a threshold at about M_L = 2.0. Moreover, the azimuthal coverage of the stations, deficient north of latitude 43°N, leads to uncertainties of the order of 5 to 10 km in this part of the Pyrenean domain, thus casting doubt on the locations of these 10 events (hence the large search radius). Furthermore, before 2018, most of the stations were operated in triggered mode, which prevents the mining of old data. Finally, there is no remnant of any waveforms prior to 1996, when new stations were installed in this part of the Pyrenean range. This is unfortunate because 8 out of the 10 potentially related events took place before 1996. Nevertheless, it was possible to examine waveforms of a M_L = 2.0 event recorded on 2011.03.30 at two permanent stations (epicentral distances of 30 and 42 km) and located only 3 km NW of the swarm, i.e. within the

location uncertainties. Both stations were still operational in 2017, and they recorded the five strongest events of the Sauveterre sequence. Although the distances were similar, the 2011 and 2017 signals did not correlate to a significant level, whereas the correlation coefficients between the 2017 events consistently exceeded 0.85. This 2011 event was the most serious candidate for a relationship with the 2017 sequence. Another one, on 2015.05.29, with huge uncertainties, failed the same type of examination at first sight. Therefore, there is no reliable record of any previous activity of the Sauveterre swarm.

Once the swarm was detected (which happened rather late), the decision was made to instrument again a site of the Maupasacq experiment (MBB11, the broadband station closest to the swarm, see Fig. 2b), with the same hardware and same implementation as during the initial deployment. This station remained in place for 4 months, from March 29th to July 7th 2018. Template matching (using the same template as in the procedure described in section 3) did not detect any activity at all. The swarm therefore died out somewhere between October 2017 and March 2018, probably closer to the beginning of this window judging by the temporal evolution of the sequence (Fig. 5). We can thus reasonably consider this activity as an exceptional episode, very fortunately recorded, which makes this sequence all the more valuable.

The question then arises as to the cause of this seismic swarm. The most universally proposed answers, in the case of "swarm" type sequences, are those of a triggering of the seismic events by acting fluids or by aseismic slip, the two mechanisms not excluding one another (e.g. Hainzl, 2004; Vidale and Shearer, 2006; Roland and McGuire, 2009; Chen et al., 2012; Daniel et al., 2011; de Barros et al., 2019). In the case of the Sauveterre swarm, the migration described earlier, of a few tens of meters over four months, categorically rules out an interpretation in terms of a classical aseismic slip as the underlying mechanism (which rather involves speeds on the order of km/h, e.g. Lohman and McGuire, 2007). In general, migration speeds in the range of meters to tens of meters per day argue for a fluid-driven mechanism, such as diffusive propagation of fluid overpressure (Vidale and Shearer, 2006; Bourouis and Cornet, 2009; Chen and Shearer, 2011; Chen et al., 2012; de Barros et al., 2019, 2020; Hatch et al., 2020). However, the slowness of the migration observed here is quite puzzling: typical speeds are indeed much higher (e.g. Daniel et al., 2011 ; Derode et al., 2023). The diffusivity value, in the order of 10^{-4} m²/s, is very small compared to expected diffusivity coefficients, usually ranging from 0.02 to about 10 m²/s (e.g. Shapiro et al., 1997, 2002). The marly nature of the geological layers that host the swarm (e.g. Saspiturry et al., 2019) might be invoked to explain such a low diffusivity.

Note that in certain contexts, stress transfer or dynamic triggering have been invoked as possible mechanisms to initiate swarm-like sequences (e.g. de Barros et al., 2019). Due to the lack of significant nearby events, such hypotheses can here be confidently ruled out.

Features of the frequency-magnitude distribution (Fig. 7) are worth discussing. For both phases of the sequence, the slopes of the distributions are on the order of 0.8, but qualifying them as b-

parameters seems hazardous due to their irregularity. These frequency-magnitude distributions are also very unusual in the absence of a plateau like those usually observed below a so-called completeness magnitude. Here, no completeness value emerges from the data, despite the fact that there are more than enough of them to base reliable calculations on (nearly 450 over the two phases). These plateaus usually mark the inability of the observation network to detect events below a certain energy threshold. Here, we have rather the impression that there is a "floor" magnitude under which no event exists, which is quite intriguing from a mechanical point of view and which certainly call for further investigations.

If we now return to figures 9 and 10, some lessons can be drawn from the observations made on the changes in the waveforms, and on the particle motion plots. The evolution of waveforms over time among a set of repeaters can have two types of causes: either geographical displacements (migration) of the sources, or changes in the propagation medium, for instance in seismic velocities (e.g. Uchida and Bürgmann, 2019) or in seismic anisotropy. In particular, we can notice that the preferential distribution of S energy in different directions (such as displayed by the particle motion plots of Fig. 10) is often related to anisotropy encountered by the waves on their path. It is therefore possible that the observations reflect changes in the anisotropic properties of the medium. On the contrary, a simple migration of events over a few tens of meters could hardly explain the observations made on late arrivals, while early arrivals do not seem to be affected (which is particularly clear on the stacked seismograms of figures 9 and S1). Note indeed that only the late phases show these changes, and that the first arrivals, direct and propagating upwards, are unchanged over time (see Fig. 9). If we assume that the late phases that undergo these changes are reflected or converted at an interface (which would be thus subject to changes over time), this seems to suggest that this structure is located under the swarm. Finally, it is interesting to consider that these observations on the late part of the seismograms can be made on station S0316 and it alone. The other nearby stations (including S0516, see Fig. 3) do not show this. This argues for a local disturbance of the medium, most likely related to crack-induced anisotropy. If this hypothesis is correct, it could suggest the drainage of fluid-filled fractures during the first phase of the swarm.

A final observation can be made in figure 9. It seems that at the end of the second phase, the 3-C waveforms of the last event return to characteristics closer to those of the first phase. It is of course difficult to draw conclusions on an isolated event, but it can be noted on the correlation matrix of figure 8 that a renewed correlation between phase 1 and the latest events is also clearly visible. This observation could suggest a periodicity in the underlying processes.

In two recent papers, Lefeuvre et al (2021, 2022) measured high concentration of natural dihydrogen leakage in the precise area of the Sauveterre swarm. They explored in detail the production of H2 and other gases (CO2, radon) on both sides of the North Pyrenean Frontal Thrust (NPFT) and highlighted a production peak at the crossing of the fault plane corresponding to one of

its secondary branches, which they interpret in terms of transport along the thrust toward the surface of hydrogen produced by serpentinization (Lefeuvre et al., 2022). Indeed, the local geology is highly favorable, with the presence of the aforementioned mantle body beneath the Mauléon basin, probably connected to the surface by at least one branch of the NPFT. Serpentinization of mantle rocks is one of the most efficient ways for the generation of abiotic dihydrogen (e.g. Klein et al., 2020), and the study area of Lefeuvre et al. (2022) is located just above (less than 1 km north) the seismic swarm. Therefore there is both a source of production and a means of transporting hydrogen. This is illustrated by the cross-section in figure 12, on which are superimposed the seismicity recorded during the Maupasacq campaign, the seismic velocity anomalies obtained through the local earthquake tomography (Villaseñor et al. 2019, Lehujeur et al., 2021), and the delineation of the main frontal thrusts.

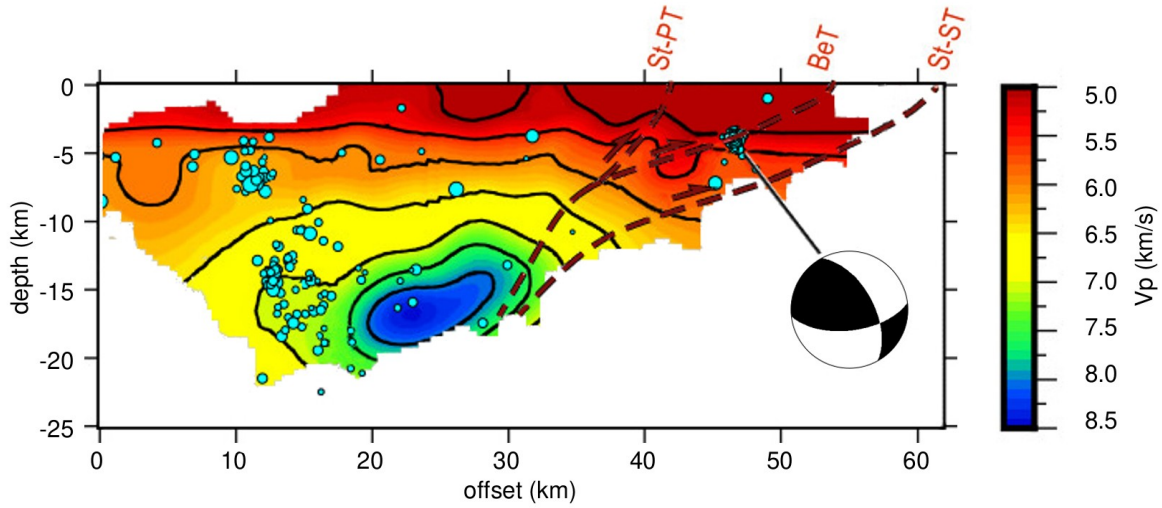

Figure 12. Cross-section in the tomographic Vp model of Lehujeur et al. (2021), with seismicity superimposed (initial location procedure, blue circles). The SSW-NNE azimuth of the cross-section is displayed on the seismicity map of figure 2. Dashed lines correspond to the main branches of the North Pyrenean Frontal Thrust as pictured in the geological literature (e.g. Saspitury et al., 2019; Lefeuvre et al., 2022). St-Pt: Saint-Palais Thrust. St-ST: Sainte-Suzanne Thrust. BeT: Bellevue Thrust. The Sauveterre swarm (before accurate relocation) shows up at offset 47 km, around 4 km depth, on the Bellevue Thrust. The focal mechanism is that of the master event of the sequence (2017.06.19-07:43), also displayed on figures 2 and 11.

It is then tempting to consider the existence of a link between our seismic swarm and this probable fluid channeling. Could the swarm reflect a burst in fluid circulation ? Could the two distinct phases and the waveform observations of figure 9, which seem to point to 3D effects and/or changes in anisotropy, reflect temporary changes in "filling" conditions of a conduit in the vicinity of the swarm ? Since the swarm is seated at 4 km depth, the shallower part of the NPFT would have to be very steep to act as a channel, probably steeper than is generally drawn in

geological cross-sections (e.g. Saspiturry et al., 2019; Lefeuvre et al., 2022), consistent with the observation of steeply dipping nodal planes in the focal mechanisms of the swarm (Fig. 11).

The many observations that can be made on this exceptional dataset also open up questions that are not addressed here, but that deserve specific future work. We see three types of questions: mechanical, dynamic and structural.

Mechanical because the recorded earthquakes have the particularity of representing a relatively large set of events extremely close to each other, captured by a large number of stations, and covering nearly three orders of magnitude. There is therefore a good opportunity to study the scaling of source parameters under conditions that allow us to get rid of a certain number of troublesome parameters such as the change in source locations or focal mechanisms. Let us recall in passing the unusual aspect of the frequency-magnitude distributions (Fig. 7) suggesting the existence of minimum values for the magnitudes of the swarm.

Dynamic, because we need to better understand the segmentation into two very distinct phases of this swarm, the brief period of quiescence that separates them, as well as the spatial migration from one to the other. The temporal variations of seismic waveforms could potentially provide key insight into the changes in medium properties and the dynamics of a seismic swarm.

Structural, as regards the numerous secondary phases visible on figures 3 and 9 and which reveal the existence of interfaces with strong contrasts within the sedimentary basin hosting the Sauveterre swarm, probably in connection with the thrust fronts described above. A precise modelling of these interfaces will allow to make advances on the detailed structure of these thrusts, which will offer an additional constraint on the pathways along which fluids come to the surface.

5 Conclusions

Thanks to a large N and T deployment in the Pyrenean foreland, we have had the opportunity to record a rare seismic sequence, with several hundreds of very small events concentrated in an extremely limited volume. Template matching, cross-correlation differential time picking, relative double difference relocation, computation of focal solutions have allowed to characterize this sequence in detail. A slow migration has been evidenced, compatible with a classical fluid-driven mechanism. However, the originality of the sequence lies in the existence of two distinct phases separated by a short seismic quiescence, revealing a small but clear geographical shift, different mechanical behaviors, and very particular changes in the waveforms of secondary arrivals which plead in favor of sudden changes in the propagation medium.

The fortuitous observation of the Sauveterre swarm is an unexpected development of the dense Maupasacq deployment. It underlines the interest of such experiments, involving a large number of

sensors recording over a long observation time, even in a context of moderate seismicity. It opens up new avenues for further development, in particular for the use of the recorded waveforms for fine imaging of the local crustal structure, and for understanding the physical processes at the origin of the swarm. In this respect, preliminary measurements of dihydrogen degassing seem to suggest the existence of deep fluid circulations, of which the swarm could be one of the manifestations.

Data and resources

The Maupasacq dataset is not yet public. However, extractions of seismograms related to the Sauveterre swarm (waveforms in SAC or SEED format) can be obtained from the authors on request.

Supplemental Material include a description of the MAUPASACQ instrumental setup and a figure showing in a different way from figure 9 (envelopes of the signal) the evolution over time of the waveforms at station S0316.

Acknowledgments

This work was supported by OROGEN, a tripartite research project involving the Centre National de la Recherche Scientifique (CNRS), Total and the Bureau de Recherches Géologiques et Minières (BRGM). We would like to thank all the members of the wonderful "Maupasacq team" whose contribution and involvement made this ambitious and innovative project possible. J-B.A. acknowledges funding from the Agencia Nacional de Investigación y Desarrollo (ANID) of Chile (FONDECYT 3200633). All the figures were made using the GMT software (Wessel and Smith, 1991). We thank two anonymous reviewers and associate editor YoungHee Kim for their insightful comments that improved the manuscript.

This work is dedicated to our colleague and friend Jean-Baptiste Ammirati, who died shortly before its completion.

References

Asensio, E., G. Khazaradze, A. Echeverria, R. W. King, R. W., and I. Vilajosana (2012). GPS studies of active deformation in the Pyrenees, *Geophys. J. Int.*, **190**, 913–921. DOI: 10.1111/j.1365-246X.2012.05525.x

Boué, P., J. Brives, L. Stehly, M. Lehujeur, S. Chevrot, M. Sylvander, and M., Collin (2019). Local ambient noise tomography using a dense array : the MAUPASACQ experiment, in: *Geophysical Research Abstracts*, Vienna, Austria, 7–12 April 2019, Vol. 21, EGU General Assembly

Bourouis, S., and F. H. Cornet (2009). Microseismic activity and fluid fault interactions: some results from the Corinth Rift Laboratory (CRL), Greece, *Geophys. J. Int.*, **178**, 561-580. DOI: 10.1111/j.1365-246X.2009.04148.x

Chen, X., and P. M. Shearer (2011). Comprehensive analysis of earthquake source spectra and swarms in the Salton Trough, California, *J. Geophys. Res.: Solid Earth*, **116**(B9). DOI: 10.1029/2011JB008263

Chen, X., P. M. Shearer, and R. E. Abercrombie (2012). Spatial migration of earthquakes within seismic clusters in Southern California: Evidence for fluid diffusion, *J. Geophys. Res.: Solid Earth*, **117**. DOI: 10.1029/2011JB008973

Chevrot, S., M. Sylvander, and B. Delouis, B. (2011). A preliminary catalog of moment tensors for the Pyrenees, *Tectonophysics*, **510**, 239–251. DOI: 10.1016/j.tecto.2011.07.011

Chevrot, S., M. Sylvander, J. Diaz, R. Martin, F. Mouthereau, G. Manatschal, E. Masini, S. Calassou, F. Grimaud, and H. Pauchet (2018). The non-cylindrical crustal architecture of the Pyrenees, *Sci. Rep.*, **8**, 9591. DOI: 10.1038/s41598-018-27889-x

Chevrot, S., M. Sylvander, A. Villaseñor, J. Diaz, L. Stehly, P. Boué, V. Monteiller, R. Martin, M. Lehujeur, S. Beller, J. Brives, A. Bitri, S. Calassou, M. Collin, M. Ford, L. Jolivet, G. Manatschal, E. Masini, F. Mouthereau, and O. Vidal (2022). Passive imaging of collisional orogens: a review of a decade of geophysical studies in the Pyrénées, *Bull. Soc. Géol. Fr.*, **193**(1). DOI:10.1051/bsgf/2021049

Daniel, G., F. Renard, F. Thouvenot, L. Jenatton, A. Helmstetter, S. Hainzl, D. Marsan, and R. Guiguet (2011). Changes in effective stress during the 2003–2004 Ubaye seismic swarm, France, *J. Geophys. Res.*, **116**, B01309. DOI:10.1029/2010JB007551

de Barros, L., M. Baques, M. Godano, A. Helmstetter, A. Deschamps, C. Larroque, and F. Courboulex (2019). Fluid-induced swarms and coseismic stress transfer: a dual process highlighted in the aftershock sequence of the 7 April 2014 earthquake (Ml 4.8, Ubaye, France), *J. Geophys. Res.*, **124**(4), 3918-3932. DOI: 10.1029/2018JB017226

de Barros, L., F. Cappa, A. Deschamps, and P. Dublanchet (2020). Imbricated aseismic slip and fluid diffusion drive aseismic swarm in the Corinth Gulf, Greece, *Geophys. Res. Lett*. DOI: 10.1029/2020GL087142

Derode, B., Gounon, A., J. Letort, M. Sylvander, A. Rigo, S. Benahmed, F. Grimaud, S. Latour, H. Pauchet, and A. Santamaria (2023). Fluid-driven seismic swarms in the Gripp valley (Haute-Pyrénées, France), *Geophys. J. Int*., **234**, 1903-1915. DOI: 10.1093/gji/ggad175

Dreger, D. S., H. Tkalčić and M. Johnston (2000). Dilational Processes Accompanying Earthquakes in the Long Valley Caldera, *Science*, **288**, 5463, 122-125. DOI: 10.1126/science.288.5463.122

Duboeuf, L., A. M. Dichiarante, and V. Oye (2022). Interplay of large-scale tectonic deformation and local fluid injection investigated through seismicity patterns at the Reykjanes Geothermal Field, Iceland, *Geophys. J. Int.* **228**, 1866–1886. DOI: 10.1093/gji/ggab423.

Duverger, C., G. Mazet-Roux, L. Bollinger, A. Guilhem Trilla, A. Vallage, B. Hernandez, and Y. Cansi (2021). A decade of seismicity in metropolitan France (2010-2019): the CEA/LDG methodologies and observations, *Bull. Soc. Géol. Fr*. DOI: 10.1051/bsgf/2021014

Fillon, C., F. Mouthereau, S. Calassou, R. Pik, N. Bellahsen, C. Gautheron, D. Stockli, S. Brichau, N. Daril, M. Mouchené, and P. van der Beek (2020). Post-orogenic exhumation in the western Pyrenees: evidence for extension driven by pre-orogenic inheritance, *J. Geol. Soc*. DOI: 10.1144/jgs2020-079

Fischer, T., J. Horálek, P. Hrubcová, V. Vavryčuk, K. Bräuer, and H. Kämpf (2014). Intra-continental earthquake swarms in West-Bohemia and Vogtland: A review, *Tectonophysics*, **611**, 1-27. DOI: 10.1016/j.tecto.2013.11.001

Hainzl, S. (2004). Seismicity patterns of earthquake swarms due to fluid intrusion and stress triggering, *Geophys. J. Int.*, **159**, 1090-1096. DOI: 10.1111/j.1365-246X.2004.02463.x

Hanks, T. C., and W. H. Bakun (2002). A bilinear source-scaling model for M-log A observations of continental earthquakes, *Bull. Seism. Soc. Am.*, **92** (5), 1841–1846. DOI: 10.1785/0120010148

Hatch, R. L., R. E. Abercrombie, C. J. Ruhl, and K. D. Smith (2020). Evidence of aseismic and fluid-driven processes in a small complex seismic swarm near Virginia City, Nevada, *Geophys. Res. Lett.*, **47**, e2019GL085477. DOI: 10.1029/2019GL085477

Heinicke, J., T. Fischer, R. Gaupp, J. Götze, U. Koch, H. Konietzky, and K.P. Stanek (2009). Hydrothermal alteration as a trigger mechanism for earthquake swarms: the Vogtland/NW Bohemia region as a case study, *Geophys. J. Int.*, **178**, 1-13. DOI: 10.1111/j.1365-246X.2009.04138.x

Hill, D. P. (1977). A model for earthquake swarms, *J. Geophys. Res*. **82**, no. 8, 1347–1352, doi: 10.1029/JB082i008p01347.

Jammes, S., G. Manatschal, L. Lavier, and E. Masini (2009). Tectonosedimentary evolution related to extreme crustal thinning ahead of a propagating ocean: Example of the western Pyrenees, *Tectonics* **28** (4), TC4012. DOI: 10.1029/2008TC002406

Klein, F., J. D. Tarnas, and W. Bach (2020). Abiotic sources of molecular hydrogen on Earth, *Elements*, **16**, no. 1, 19–24, doi: 10.2138/gselements.16.1.19.

Krischer, L., T. Megies, R. Barsch, M. Beyreuther, T. Lecocq, C. Caudron, and J. Wassermann (2015). ObsPy : a bridge for seismology into the scientific Python ecosystem, *Comput. Sci. Discov.* **8**, 014003. DOI: 10.1088/1749-4699/8/1/014003

Lacan P., and M. Ortuño (2012). Active tectonics in the Pyrenees: A review, *J. Iberian.Geol.* **38**, 9-30. DOI: 10.5209/rev_JIGE.2012.v38.n1.39203

Lee, W. H. L. and J. C. Lahr (1975). HYPO71 (revised) a computer program for determining hypocenter, magnitude, and first motion pattern of local earthquakes, Open-File Report 75-311, U.S. Geological Survey. DOI: 10.3133/ofr75311

Lefeuvre, N., L. Truche, F.-V. Donzé, M. Ducoux, G. Barré, R.-A. Fakoury, S. Calassou, and E. C. Gaucher (2021). Native H2 exploration in the western pyrenean foothills, *G-cubed*, **22**, 8. DOI: 10,1029/2021GC009917

Lefeuvre, N., L. Truche, F.-V. Donzé, F. Gal, J. Tremosa, R.-A. Fakoury, S. Calassou, and E. C. Gaucher (2022). Natural hydrogen migration along thrust faults in foothill basins: The North Pyrenean Frontal Thrust case study, *Appl. Geochem.,* **145:**105396-105396. DOI: 10.1016/j.apgeochem.2022.105396

Lehujeur, M., S. Chevrot, A. Villaseñor, E. Masini, N. Saspiturry, R. Lescoutre, and M. Sylvander (2021). Three-dimensional shear velocity structure of the Mauléon and Arzacq Basins (Western Pyrenees), *Bull. Soc. Géol. Fr.*, **191**(1). DOI:10.1051/bsgf/2021039

Lescoutre, R., and G. Manatschal (2020). Role of rift-inheritance and segmentation for orogenic evolution: example from the Pyrenean-Cantabrian system, *Bull. Soc. Géol. Fr.*, **191**(18). DOI:10.1051/bsgf/2020021

Lohman, R. B., and J. J. McGuire, (2007). Earthquake swarms driven by aseismic creep in the Salton Trough, California, *J. Geophys. Res.*, **112**, B04405. DOI: 10.1029/2006JB004596

Lois, A., E. Sokos, N. Martakis, P. Paraskevopoulos, and G.-A. Tselentis (2013). A new automatic S-onset detection technique: Application in local earthquake data, *Geophysics,* **78**(1): KS1–KS11. DOI: 10.1190/geo2012-0050.1

Masini, E., G. Manatschal, J. Tugend, G. Mohn, and J.-M. Flament (2014). The tectono-sedimentary evolution of a hyper-extended rift basin: the example of the Arzacq–Mauléon rift system (Western Pyrenees, SW France), *Int. J. Earth Sci.*, **103** (6), pp. 1569-1596. DOI: 10.1007/s00531-014-1023-8

Masson, C., S. Mazzotti, P. Vernant, and E. Doerflinger (2019). Extracting small deformation beyond individual station precision from dense GNSS networks in France and Western Europe, *Solid Earth*, **10**, 1905–1920.DOI: 10.5194/se-10-1905-2019

Mazzotti, S., C. Aubagnac, L. Bollinger, K. Coca Oscanoa, B. Delouis, D. Do Paco, C. Doubre, M. Godano, H. Jomard, C. Larroque, A. Laurendeau, F. Masson, M. Sylvander, and A. Trilla (2021). FMHex20: An earthquake focal mechanism database for seismotectonic analyses in metropolitan France and bordering regions, *Bull. Soc. Géol. Fr.*, **192**(1), 10. DOI: 10.1051/bsgf/2020049

Mogi, K. (1963). Some discussions on aftershocks, foreshocks and earthquake swarms — the fracture of semi-infinite body caused by an inner stress origin and its relation to the earthquake phenomena, *Bull. Earthq. Res. Inst.*, **41,** 615-658

Mouthereau, F., P.-Y. Filleaudeau, A. Vacherat, R. Pik, O. Lacombe, M.G. Fellin, S. Castelltort, F. Christophoul, and E. Masini (2014). Placing limits to shortening evolution in the Pyrenees: Role of margin architecture and implications for the Iberia/Europe convergence, *Tectonics*, Vol **33**, Issue 12. DOI: 10.1002/2014TC003663

Nocquet, J.-M (2012). Present-day kinematics of the Mediterranean: a comprehensive overview of GPS results, *Tectonophysics*, **579**, 220–242. DOI: 10.1016/j.tecto.2012.03.037

Polychronopoulou, K., A. Lois, N. Martakis, S. Chevrot, M. Sylvander, J. Diaz, and A. Villaseñor (2018). Broadband, short-period or geophone nodes? Quality assessment of passive seismic signals acquired during the Maupasacq experiment, *First Break,* **36**, no. 4, 71–76, doi: 10.3997/1365-2397.n0085.

Rigo A., P. Vernant, K. L. Feigl, X. Goula, G. Khazaradze, J. Talaya, L. Morel, J. Nicolas, S. Baize, J. Chéry, and M. Sylvander (2015). Present-day deformation of the Pyrenees revealed by GPS surveying and earthquake focal mechanisms until 2011, *Geophys. J. Int.*, **201**:947–964. DOI: 10.1093/gji/ggv052

Roland, E., and J. McGuire (2009). Earthquake swarms on transform faults, *Geophys. J. Int.,* **178**, 1677–1690, doi: 10.1111/j.1365-246X.2009.04214.x.

Saspiturry, N., P. Razin, T. Baudin, O. Serrano, B. Issautier, E. Lasseur, C. Allanic, I. Thinon, and S. Leleu (2019). Symmetry vs. asymmetry of a hyper-thinned rift: Example of the Mauléon Basin (Western Pyrenees, France), *Mar. Petrol. Geol*., **104**, 86-105. DOI:10.1016/ j.marpetgeo.2019.03.031

Shapiro, S. A., E. Huenges, and G. Borm (1997). Estimating the crust permeability from fluid-injection-induced seismic emission at the KTB site, *Geophys. J. Int.*, **131**, F15-F18. DOI: 10.1111/j.1365-246X.1997.tb01215.x

Shapiro, S., E. Rothert, V. Rath, and J. Rindschwentner (2002). Characterization of fluid transport properties of reservoirs using induced microseismicity, *Geophysics*, **67**, 1, pp. 212-220. DOI:10.1190/1.1451597

Snoke, J. A. (2003). FOCMEC: FOcal MEChanism determinations, International Hand-book of Earthquake and Engineering Seismology (Lee, Kanamori, Jennings and Kisslinger, eds.), Academic Press, San Diego (Part B: 1629-1630). http://www.iris.edu/pub/programs/focmec/

Souriau, A., and H. Pauchet (1998). A new synthesis of Pyrenean seismicity and its tectonic implications, *Tectonophysics*, **290**, 221–244. DOI: 10.1016/S0040-1951(98)00017-1

Souriau, A., M. Sylvander, A. Rigo, J.-F. Fels, J.-M. Douchain, and C. Ponsolles (2001). Sismotectonique des Pyrénées: principales contraintes sismologiques, *Bull. Soc. Géol. Fr*., **172**, 25-39. DOI: 10.1016/S0040-1951(98)00017-1

Sylvander, M., A. Rigo, G.. Sénéchal, J. Battaglia, S. Benahmed, M. Calvet, S. Chevrot, J.-M. Douchain, F. Grimaud, J. Letort, and H. Pauchet (2021). Seismicity patterns in southwestern France, *CR Geoscience*, **353**(S1), 1-26. DOI: 10.5802/crgeos.60

Tselentis, G.-A., N. Martakis, P. Paraskevopoulos, A. Lois, and E. Sokos (2011). A method for microseismic event detection and P-phase picking, in *SEG Technical Program Expanded Abstracts* 2011. Society of Exploration Geophysicists, Houston, Texas

Uchida, N., and R. Bürgmann (2019). Repeating earthquakes, *Annu. Rev. Earth Planet. Sci.*, **47**, 305-332. DOI: 10.1146/annurev-earth-053018-060119

Vidale, J. E., and P. M. Shearer, P. M. (2006). A survey of 71 earthquake bursts across southern California: Exploring the role of pore fluid pressure fluctuations and aseismic slip as drivers. *J. Geophys. Res.: Solid Earth*, **111**(B5). DOI: 10.1029/2005JB004034

Villaseñor, A., S. Chevrot, M. Sylvander, K. Polychronopoulou, N. Martakis, M. Collin, et al. (2019). Crustal architecture of the Mauleon Basin (Western Pyrenees) from high resolution local earthquake tomography using the large-N Maupasacq experiment. In: *Geophysical Research Abstracts*, Vienna, Austria, 7–12 April 2019, Vol. **21**, EGU General Assembly

Waldhauser, F. (2001). HypoDD: A computer program to compute double-difference earthquake locations, *U.S. Geol. Survey Open-File Rept*, 01-113, 25 pp, available at https://pubs.usgs.gov/of//2001/0113 (last accessed June 2023).

Waldhauser, F., and W. Ellsworth (2000). A Double-Difference Earthquake Location Algorithm: Method and Application to the Northern Hayward Fault, California, *Bull. Seism. Soc. Am.,* **90 (**6), 1353–1368. DOI: 10,1785/0120000006

Wang, Y., S. Chevrot, V. Monteiller, D. Komatitsch, F. Mouthereau, G. Manatschal, M. Sylvander, J. Diaz, M. Ruiz, F. Grimaud, S. Benahmed, H. Pauchet, R. Martin (2016). The deep roots of the western Pyrenees revealed by full waveform inversion of teleseismic P waves, *Geology*, **44**, 475-478. DOI: 10.1130/G37812.1

Wei, S., J.-P. Avouac, K. W. Hudnut, A. Donnellan, J. W. Parker, R. W. Graves, D. Helmberger, E. Fielding, Z. Liu, F. Cappa and M. Eneva (2015). The 2012 Brawley swarm triggered by injection-induced aseismic slip, *Earth Planet. Sci. Lett*., 422, 115-225. DOI: 10.1016/j.epsl.2015.03.054

Wessel, P., and W.H.F. Smith (1991). Free software helps map and display data, *EOS Trans. Am. Geophys. Un.*, **72**(41), 441–446. DOI: 10.1029/90EO00319

Wiemer, S. and M. Wyss (1997). Mapping the Frequency-Magnitude Distribution in Asperities: An Improved Technique to Calculate Recurrence Times? *J. Geophys. Res.*, 102, 15115-15128. DOI: 10.1029/97JB00726

Wiemer, S. and M. Wyss (2000). Minimum Magnitude of Completeness in Earthquake Catalogs: Examples from Alaska, the Western United States, and Japan, *Bull. Seism. Soc. Am*., **90**, 859-869. DOI:10.1785/0119990114

Wyss, M., K. Shimazaki and S. Wiemer (1997). Mapping active magma chambers by b values beneath the off-Ito volcano, Japan, *J. Geophys. Res.*, **102**, B9, 20413-20422. DOI: 10.1029/97JB01074

Yamashita, T. (1999). Pore creation due to fault slip in a fluid-permeated fault zone and its effect on seismicity: generation mechanism of earthquake swarm. *Pure appl. Geophys.*, **155**(2–4), 625–647. DOI: 10.1007/s000240050280

AUTHORS' ADDRESSES

Matthieu Sylvander (1) msylvander@irap.omp.eu
Sébastien Chevrot (2) sebastien.chevrot@get.omp.eu
Jean-Baptiste Ammirati (2,3) deceased March 2023
Sylvain Calassou (4) sylvain.calassou@total.com
Magali Collin (4) magali.collin@total.com
Jordi Diaz (5) jdiaz@ictja.csic.es
Nikos Martakis (6) nmartakis@seismotech.gr
Katerina Polychronopoulou (6) kpolychro@seismotech.gr
Antonio Villaseñor (7) antonio.villasenor@csic.es

1- IRAP, UMR 5277, Université de Toulouse, CNRS, CNES, UPS (Toulouse), France
2- GET, UMR 5563, Université Paul Sabatier, CNRS, IRD, Toulouse, France
3- Departamento de Geología, Universidad de Chile, Plaza Ercilla 803, 8320000, Santiago, Chile
4- TOTAL EP/R&D, Pau, France
5- Geosciences Barcelona, CSIC, Barcelona, Spain
6- Seismotech SA, Athens, Greece
7- Institut de Ciències del Mar, Barcelona, Spain

SUPPLEMENTAL MATERIAL

This supplemental material includes two items:

- A text describing the MAUPASACQ passive deployment.

- A figure (S1) with envelopes of 3C-waveforms for station S0316, showing changes over time. It complements figure 9 of the manuscript.

The Maupasacq experiment.

The Maupasacq experiment was designed so as to make it a rare example of long-term continuous monitoring with a large number of sensors over an intermediate-size zone with natural, moderate seismicity. A network of 452 three-component seismic stations was deployed and maintained in a 50x30 km² area during 6 months (March-September 2017). The design of the experiment consisted of three nested arrays mixing instruments with different bandwidths (Fig. 1c): broadband sensors (Güralp CMG40-T and Trillium 120 compact), short-period sensors at 1Hz (Seismotech SA design), and Sercel nodes at 8.5 Hz. The broadband deployment took the form of a 2D rectangular grid with a 7 km spacing, surrounded by a looser ring to mitigate edge effects during tomographic inversions. The broadband grid was densified by another regular short-period grid (3 km interstation spacing), itself completed by 5 rows and 3 columns of nodes, resulting in lines with a spacing of 1 km between sensors. The stations were set up autonomously, without communication links and without external power supply - except for the broadband stations, which were powered by AC or solar energy. Most sites were therefore visited several times during the experiment, for battery replacement and memory download, by a team of 6 persons specially hired for the duration of the experiment. Due to the differences in operating systems and native formats, only limited quality control was performed during the Maupasacq experiment, and the first comprehensive data work did not take place until a few weeks after the instruments were dismantled.

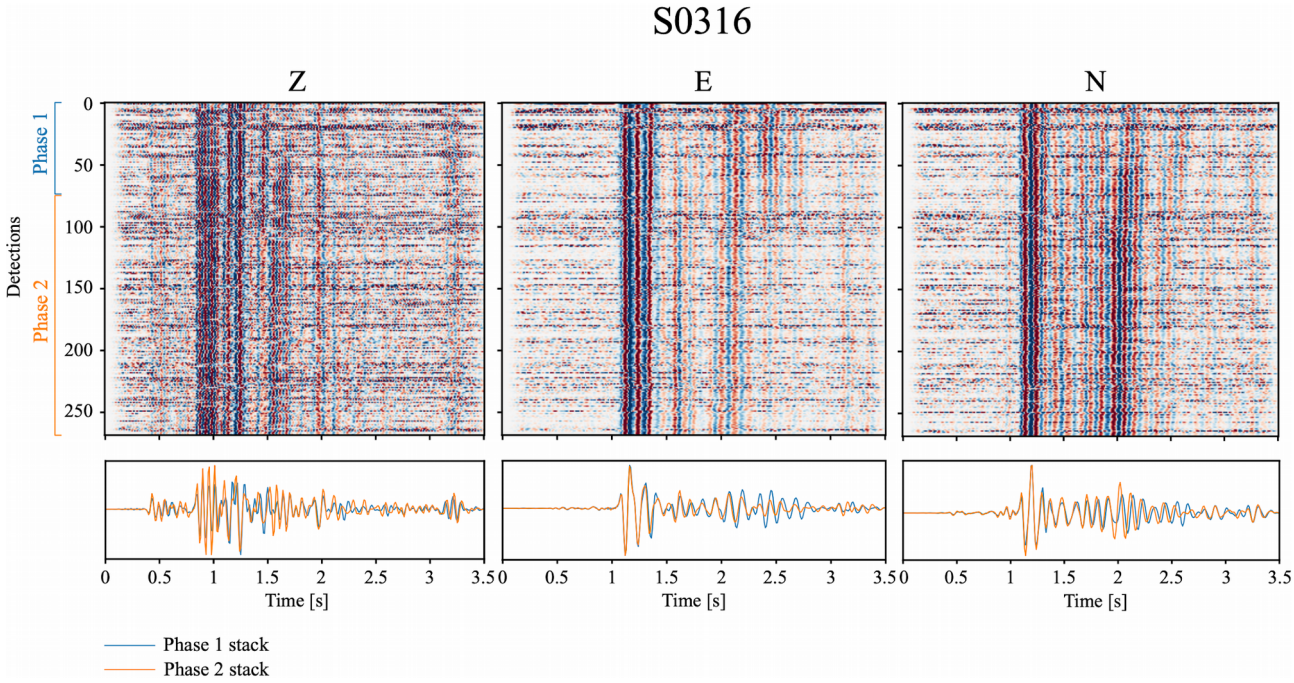

Figure S1. Top row: three-component waveforms (envelopes) of all events identified by template matching at station S0316 (see Fig. 9); the waveforms are arranged in chronological order (earliest at the top), normalized to the maximum amplitude of the trace and aligned to origin time. Bottom row: stacked waveforms (time series) for the two phases of the sequence.